2014 IEEE International Conference on Robotics & Automation (ICRA)
Hong Kong Convention and Exhibition Center
May 31 - June 7, 2014. Hong Kong, China

Design Optimization of a Bone-Attached, Redundant and Reconfigurable Parallel Kinematic Device for Skull Surgery

Jan-Philipp Kobler[1], Jens Kotlarski[1], G. Jakob Lexow[2], Omid Majdani[2], and Tobias Ortmaier[1]

Abstract— **Bone-attached robots and so-called microstereotactic frames are attracting increasing interest in the field of robot-assisted surgery due to the promising targeting accuracy they provide. The authors propose a passive Stewart-Gough platform which is attached to a patient's head via bone anchors. It serves as an instrument guidance in straight line incisions, such as minimally invasive cochlear implantation. In this contribution a modified version of the mechanism's kinematics is proposed, which reduces the number of required bone anchors from six to three. Furthermore, a novel statistical approach to optimize the design variables of the moving platform for accuracy is presented. It is characterized by the ability to take the probability distributions of all relevant error sources as well as the given task redundancy and reconfigurability of the mechanism into account. Based on identified ranges of trajectories and possible bone anchor locations, the optimization problem is solved for a representative number of 1,000 'virtual patients'. The optimum mechanism design is obtained by analyzing the resulting distributions of design variables. Monte Carlo simulation is used to compare its targeting errors to those of a previous prototype. Results reveal that the targeting error is significantly reduced in comparison to an initial prototype thanks to the proposed optimization strategy.**

I. INTRODUCTION

Cochlear implants can restore partial hearing to patients suffering from severe hearing loss or deafness. The state of the art surgical procedure comprises gaining access to the inner ear (mastoidectomy), opening of the cochlea (cochleostomy), and inserting an electrode in order to electrically stimulate the auditory nerve. For the purpose of reducing patients' trauma, several research groups propose a minimally invasive approach by drilling a canal from the lateral skull base to the basal turn of the cochlea [1], [2], [3], [4]. Due to the fact that the required targeting accuracy is at least $0.5\,\mathrm{mm}$, the direct cochlear access is considered as a benchmark application for means of instrument guidance [5]. Vital structures, such as the facial nerve and the chorda tympani, are located in direct proximity to the drill trajectory, thus increasing the demands on accuracy. Recently, bone-attached robots and so-called microstereotactic frames have demonstrated promising target accuracies [6], [7], [8]. Such devices are attached directly to a patient's skull via bone anchors and provide instrument guidance along a predefined, straight line trajectory.

This work was funded by the German Research Foundation (DFG).

[1]Jan-Philipp Kobler, Jens Kotlarski, and Tobias Ortmaier are with the Institute of Mechatronic Systems, Leibniz Universität Hannover, 30167 Hannover, Germany. jan-philipp.kobler@imes.uni-hannover.de

[2]G. Jakob Lexow and Omid Majdani are with Hannover Medical School, Department of Otolaryngology, 30625 Hannover, Germany. lexow.jakob@mh-hannover.de

In this context, the authors propose a passive Stewart-Gough platform, which requires six bone screws, implanted at locations with appropriate skull thickness, as base joints [9]. Spherical heads of the bone anchors serve as artificial landmarks during trajectory planning, which is carried out based on a Computed Tomography (CT) scan of the patient's skull. Since no fixation frame is required, intervention planning flexibility is increased compared to similar approaches. Considering the drilling task, two redundant degrees of freedom, i.e., platform height and rotation around the drill axis, can be exploited during the preoperative planning phase in order to optimize certain performance indices of the manipulator with respect to stiffness and singularity avoidance. Furthermore, the mechanism can be reconfigured due to redundant joint connections. A detailed description of the intended surgical workflow can be found in [9].

In order to reduce the invasiveness of the procedure, a modified kinematic concept of the parallel mechanism, which brings the number of required bone anchors down to three, is introduced in this paper. Furthermore, to maximize the targeting accuracy of the robot, an optimization of the kinematic design parameters is proposed in this contribution.

So far, several researchers have reported on the design optimization of parallel kinematic machines (PKMs) for accuracy [10], [11], [12], [13]. With respect to the here considered drilling task, the common approaches are not suitable due to the following limitations. Firstly, the locations of the base joints (bone anchors) vary strongly depending on a patient's anatomy. As a result, the workspace of the PKM is specific to each surgical procedure, and thus can not be generalized appropriately for design optimization. Secondly, the optimization approaches found in the literature do not take into account the given task redundancy and reconfigurability. Therefore, a novel statistical approach to the design optimization of a redundant and reconfigurable mechanism is presented.

The remainder of this paper is organized as follows: Sect. II presents the proposed manipulator as well as a kinematic concept to reduce the number of required bone anchors from six to three. A kinematic error model, which takes into account all relevant error sources affecting the targeting accuracy of the mechanism, is introduced in Sect. III. Furthermore, an appropriate criterion to optimize the design variables for accuracy is derived, considering the specific requirements of the proposed surgical application. In order to solve the optimization problem, a novel strategy based on a statistic representation of the entire input data is presented. It allows to take into account the given task redundancy

and reconfigurability during optimization. The results of the proposed procedure are given in Sect. IV, followed by an approach to determine the achievable targeting accuracy before and after optimization. Sect. V closes the paper and gives an outlook on future work.

II. Inverse Kinematics of the 6UPS Parallel Robot

The proposed concept is based on a reconfigurable 6UPS PKM which is similar to the well-known Stewart-Gough platform (see Fig. 1). The pose (position and orientation) of the moving platform is given by

$$\boldsymbol{x}_\mathrm{E} = (x_\mathrm{E},\, y_\mathrm{E},\, z_\mathrm{E},\, \alpha_\mathrm{E},\, \beta_\mathrm{E},\, \gamma_\mathrm{E})^\mathrm{T}, \tag{1}$$

where x_E, y_E, and z_E represent the point of origin of $(\mathrm{CF})_\mathrm{E}$ with respect to $(\mathrm{CF})_0$ and α_E, β_E, and γ_E are its orientation around the x-, y-, and z-axis, respectively. In order to facilitate the here considered optimization procedure, $(\mathrm{CF})_\mathrm{E}$ is assumed at the target point t of the drill trajectory. A passive prismatic joint (linear bearing) holding a surgical tool is mounted on the moving platform, being aligned with the z-axis of $(\mathrm{CF})_\mathrm{E}$. The location of the drilling axis with respect to the center of the moving platform is characterized by a_x and a_y. The pose of the platform can be adjusted by changing the strut lengths ρ_i. The system input is given by the six actuator coordinates

$$\boldsymbol{\theta} = (\rho_1,\, \rho_2,\, \rho_3,\, \rho_4,\, \rho_5,\, \rho_6)^\mathrm{T}. \tag{2}$$

With respect to the considered drilling application γ_E is a redundant degree of freedom (DOF), i.e., not necessarily required (task redundancy). The same holds for the platform height h_P, which is defined as the distance of the platform from the entry point e in z-direction of $(\mathrm{CF})_0$. Reconfigurability is implemented by providing redundant, i.e., additional, joint connections P_7, P_8, and P_9 at the moving platform. Hence, multiple possibilities of connecting the base joints G_i to the joints at the platform P_i (strut-joint pairings $\mathbf{P}_\mathrm{sel} = (i_{\mathrm{G}_1}, \cdots, i_{\mathrm{G}_6})$) exist. Here, i_{G_1} denotes the index i of P_i being connected to G_1. This results in a large number of different configurations of the mechanism suitable for the same trajectory. The platform joints are arranged on a circle characterized by the radius r_P.

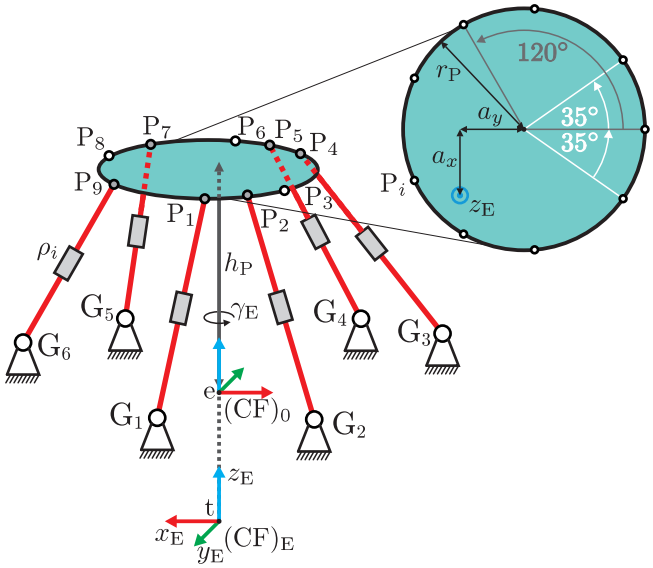

Fig. 1. Reconfigurable 6UPS parallel robot (left) and close-up top view of the moving platform (right)

In vector form, the geometric constraints of the 6UPS mechanism can be written as

$${}_{(0)}\boldsymbol{r}^{(0)}_{\mathrm{G}_i} + {}_{(0)}\boldsymbol{r}^{(\mathrm{G}_i)}_{\mathrm{P}_i} - {}_{(0)}\boldsymbol{r}^{(0)}_{\mathrm{P}_i} = \mathbf{0}, \tag{3}$$

where ${}_{(0)}\boldsymbol{r}^{(\mathrm{G}_i)}_{\mathrm{P}_i}$ is a vector given in $(\mathrm{CF})_0$ and connecting point G_i to point P_i. The remaining vectors given in (3) are equivalent to the latter explained. The positions of the passive joints P_i at the moving platform with respect to $(\mathrm{CF})_0$ are defined as

$${}_{(0)}\boldsymbol{r}^{(0)}_{\mathrm{P}_i} = {}_{(0)}\boldsymbol{x}_\mathrm{E} + {}^0\boldsymbol{R}_\mathrm{E}\, {}_{(\mathrm{E})}\boldsymbol{r}^{(\mathrm{E})}_{\mathrm{P}_i}, \tag{4}$$

where ${}^0\boldsymbol{R}_\mathrm{E}$ is the Euler rotation matrix including a rotation around the z-, the new y-, and the newest x-axis:

$${}^0\boldsymbol{R}_\mathrm{E} = \boldsymbol{R}_z(\gamma_\mathrm{E})\, \boldsymbol{R}_y(\beta_\mathrm{E})\, \boldsymbol{R}_x(\alpha_\mathrm{E}). \tag{5}$$

The Euclidean norm of the vector connecting point G_i to point P_i represents the length ρ_i of each kinematic chain i, i.e., the solution of the inverse kinematics $\boldsymbol{\theta} = \boldsymbol{h}(\boldsymbol{x}_\mathrm{E})$. Using (4) and (3) yields:

$$\rho_i = \left\| {}_{(0)}\boldsymbol{r}^{(0)}_{\mathrm{P}_i} - {}_{(0)}\boldsymbol{r}^{(0)}_{\mathrm{G}_i} \right\|_2. \tag{6}$$

The previously proposed concept of the parallel mechanism requires six bone anchors implanted in a patient's skull. In order to reduce the invasiveness and the number of incisions, a modified version of the kinematics is introduced, which brings the number of required bone anchors down to three.

The main idea is to connect two struts using a rotational joint having one degree of freedom (DOF) as depicted in Fig. 2. Compared to the well-known Stewart-Gough platform, the number of platform joints remains unchanged. Furthermore, the mechanism maintains six DOF at the moving platform. The inverse kinematics problem is solved by introducing two parameters x_v and y_v to characterize the displacement of the rotational joint G_{i+1} with respect to the spherical base joint G_i. Due to the design modifications, the base joint G_{i+1} $(i = 1, 3, 5)$ lies in the plane defined by the known positions of G_i, P_{i+1}, and P_i. Its location can be computed by applying a translation of x_v, y_v in the aforementioned plane (see also Fig. 2, red plane). Once the locations of G_2, G_4, and G_6 have been computed, the solution of the inverse kinematics problem is given by (6).

By differentiating (6) with respect to time [14], the velocity equation

$$\frac{\partial \boldsymbol{f}}{\partial \boldsymbol{x}_\mathrm{E}}\, \dot{\boldsymbol{x}}_\mathrm{E} + \frac{\partial \boldsymbol{f}}{\partial \boldsymbol{\theta}}\, \dot{\boldsymbol{\theta}} = \mathbf{0} \;\Leftrightarrow\; \boldsymbol{A}\, \dot{\boldsymbol{x}}_\mathrm{E} + \boldsymbol{B}\, \dot{\boldsymbol{\theta}} = \mathbf{0} \tag{7}$$

is obtained, where $\boldsymbol{f}$ is a 6-dimensional vector including the geometric constraints of each kinematic chain. Equation (7)

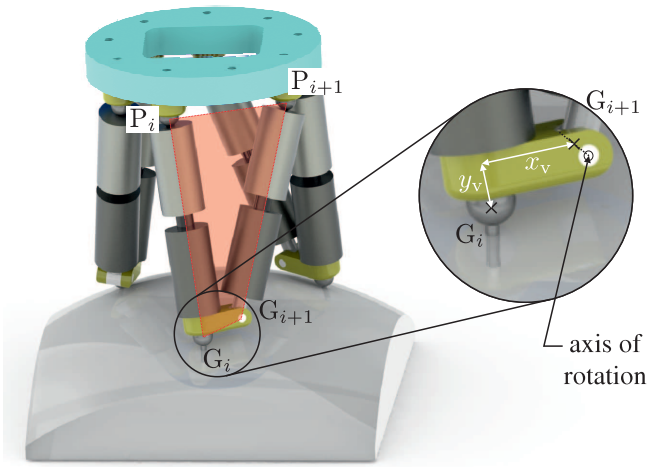

Fig. 2. Reducing the number of required bone anchors from six to three. The red plane being defined by the known positions of G_i, P_{i+1}, and P_i is used to compute the location of base joint G_{i+1}.

describes the relationship between the input $\dot{\boldsymbol{\theta}}$ and the output $\dot{\boldsymbol{x}}_{\mathrm{E}}$ velocities of a PKM, i.e., the Jacobians of the direct $\boldsymbol{A}$ and of the inverse kinematics $\boldsymbol{B}$. For the given case, the Jacobian $\boldsymbol{A} \in \mathbb{R}^{6\times 6}$ and its elements result to

$$\boldsymbol{A} = \left(\boldsymbol{c}_1^{\mathrm{T}},\ \boldsymbol{c}_2^{\mathrm{T}},\ \ldots,\ \boldsymbol{c}_6^{\mathrm{T}}\right)^{\mathrm{T}}, \tag{8}$$

with

$$\boldsymbol{c}_i = \begin{pmatrix} {}_{(0)}\boldsymbol{r}_{\mathrm{P}_i}^{(0)} - {}_{(0)}\boldsymbol{r}_{\mathrm{G}_i}^{(0)} \\ {}^0\boldsymbol{R}_{\mathrm{E}}\,{}_{(\mathrm{E})}\boldsymbol{r}_{\mathrm{P}_i}^{(\mathrm{E})} \times \left({}_{(0)}\boldsymbol{r}_{\mathrm{P}_i}^{(0)} - {}_{(0)}\boldsymbol{r}_{\mathrm{G}_i}^{(0)}\right) \end{pmatrix}.$$

The diagonal elements of the inverse kinematics Jacobian $\boldsymbol{B} \in \mathbb{R}^{6\times 6}$ are given by:

$$b_{i,i} = -\rho_i. \tag{9}$$

All the remaining elements of $\boldsymbol{B}$ are equal zero. As long as the Jacobian $\boldsymbol{A}$ is nonsingular, its inverse $\boldsymbol{A}^{-1}$ and, therefore, the overall Jacobian $\boldsymbol{J}$ can be determined (cp. (7)):

$$-\boldsymbol{B}\,\dot{\boldsymbol{\theta}} = \boldsymbol{A}\,\dot{\boldsymbol{x}}_{\mathrm{E}} \quad \Leftrightarrow \quad \dot{\boldsymbol{x}}_{\mathrm{E}} = -\boldsymbol{A}^{-1}\,\boldsymbol{B}\,\dot{\boldsymbol{\theta}} = \boldsymbol{J}\,\dot{\boldsymbol{\theta}}. \tag{10}$$

III. Design Optimization for Accuracy

A. Kinematic error model

Due to several factors, like manufacturing errors, joint clearance and limited encoder resolution, the pose of the moving platform can only be provided within a certain accuracy. Referring to [15], the active joint errors $\Delta\boldsymbol{\theta}$ are the major sources of error in a calibrated and precisely manufactured parallel mechanism. An approximation of the pose error

$$\Delta\boldsymbol{x}_{\mathrm{E}} = (\Delta x_{\mathrm{E}},\ \Delta y_{\mathrm{E}},\ \Delta z_{\mathrm{E}},\ \Delta\alpha_{\mathrm{E}},\ \Delta\beta_{\mathrm{E}},\ \Delta\gamma_{\mathrm{E}})^{\mathrm{T}} \tag{11}$$

resulting from the limited encoder resolution of the struts $\Delta\boldsymbol{\theta}$ can be obtained by rewriting the velocity equation (7) in incremental form [15]:

$$\Delta\boldsymbol{x}_{\mathrm{E}} = \boldsymbol{J}\,\Delta\boldsymbol{\theta}. \tag{12}$$

However, as simulation results reveal [9], the performance of the proposed mechanism is limited by errors occurring during the localization of its base joints G_i in preoperatively acquired CT images. Therefore, the differential kinematics formulation (12) is extended in order to take such errors into account. Furthermore, erroneous locations of the platform joints P_i, resulting from manufacturing tolerances, are considered. This is achieved by defining three error vectors

$$\Delta\boldsymbol{\theta} = (\Delta\rho_1, \Delta\rho_2, \Delta\rho_3, \Delta\rho_4, \Delta\rho_5, \Delta\rho_6)^{\mathrm{T}}, \tag{13}$$

$$\begin{aligned}\Delta\boldsymbol{r}_{\mathrm{P}} &= \left(\Delta\boldsymbol{r}_{\mathrm{P}_1}^{\mathrm{T}}, \Delta\boldsymbol{r}_{\mathrm{P}_2}^{\mathrm{T}}, \ldots, \Delta\boldsymbol{r}_{\mathrm{P}_6}^{\mathrm{T}}\right)^{\mathrm{T}} \\ &= (\Delta\mathrm{P}_{1,x}, \Delta\mathrm{P}_{1,y}, \Delta\mathrm{P}_{1,z}, \ldots)^{\mathrm{T}} \in \mathbb{R}^{18\times 1},\end{aligned} \tag{14}$$

$$\begin{aligned}\Delta\boldsymbol{r}_{\mathrm{G}} &= \left(\Delta\boldsymbol{r}_{\mathrm{G}_1}^{\mathrm{T}}, \Delta\boldsymbol{r}_{\mathrm{G}_2}^{\mathrm{T}}, \ldots, \Delta\boldsymbol{r}_{\mathrm{G}_6}^{\mathrm{T}}\right)^{\mathrm{T}} \\ &= (\Delta\mathrm{G}_{1,x}, \Delta\mathrm{G}_{1,y}, \Delta\mathrm{G}_{1,z}, \ldots)^{\mathrm{T}} \in \mathbb{R}^{18\times 1},\end{aligned} \tag{15}$$

including strut length errors $\Delta\rho_i$ as well as joint location errors at the base $\Delta\boldsymbol{r}_{\mathrm{G}_i}$ and the moving platform $\Delta\boldsymbol{r}_{\mathrm{P}_i}$, respectively. The latter are rearranged as follows:

$$\Delta\boldsymbol{C} = \left(\Delta\boldsymbol{r}_{\mathrm{P}_1}^{\mathrm{T}},\ \Delta\boldsymbol{r}_{\mathrm{G}_1}^{\mathrm{T}},\ \Delta\boldsymbol{r}_{\mathrm{P}_2}^{\mathrm{T}},\ \ldots,\ \Delta\boldsymbol{r}_{\mathrm{G}_6}^{\mathrm{T}}\right)^{\mathrm{T}}, \tag{16}$$

where $\Delta\boldsymbol{C} \in \mathbb{R}^{36\times 1}$. In order to obtain the resulting pose error of the end effector, a mapping from joint errors to strut length errors is defined by the matrix

$$\boldsymbol{N} = \begin{pmatrix} \boldsymbol{e}_{r_1}^{\mathrm{T}}\,{}^0\boldsymbol{R}_{\mathrm{E}} & -\boldsymbol{e}_{r_1}^{\mathrm{T}} & \cdots & \boldsymbol{0} & \boldsymbol{0} \\ \vdots & \vdots & \ddots & \vdots & \vdots \\ \boldsymbol{0} & \boldsymbol{0} & \cdots & \boldsymbol{e}_{r_6}^{\mathrm{T}}\,{}^0\boldsymbol{R}_{\mathrm{E}} & -\boldsymbol{e}_{r_6}^{\mathrm{T}} \end{pmatrix}, \tag{17}$$

where $\boldsymbol{e}_{r_i} \in \mathbb{R}^{3\times 1}$ is a unit vector along the strut direction and $\boldsymbol{N} \in \mathbb{R}^{6\times 36}$. Using (17), the pose error of the end effector subject to the error sources $\Delta\boldsymbol{\theta}$ and $\Delta\boldsymbol{C}$ can then be expressed as

$$\Delta\boldsymbol{x}_{\mathrm{E}} = \boldsymbol{J}(\Delta\boldsymbol{\theta} - \boldsymbol{N}\Delta\boldsymbol{C}). \tag{18}$$

Equation (18) can be reformulated in matrix form as

$$\Delta\boldsymbol{x}_{\mathrm{E}} = \boldsymbol{K}\Delta\boldsymbol{e}, \tag{19}$$

being

$$\boldsymbol{K} = (\boldsymbol{J},\ -\boldsymbol{J}\boldsymbol{N}) \in \mathbb{R}^{6\times 42}$$

commonly referred to as the total Error Transformation Matrix (ETM) and

$$\Delta\boldsymbol{e} = \begin{pmatrix} \Delta\boldsymbol{\theta} \\ \Delta\boldsymbol{C} \end{pmatrix} \in \mathbb{R}^{42\times 1}$$

the error source vector. A more detailed derivation of (18) can be found in [16] and [17].

B. Optimization problem

In the following, an optimization criterion for accuracy is derived from the kinematic error model presented in Sect. III-A. Considering the proposed surgical procedure, it is desirable to minimize the deviation from the desired trajectory at the target point $\boldsymbol{r}_{\mathrm{t}}$. Due to the fact that the

origin of $(\mathrm{CF})_{\mathrm{E}}$ equals $\boldsymbol{r}_{\mathrm{t}}$, the position error at the target results to:

$$\Delta \boldsymbol{r}_{\mathrm{t}} = \left\| \begin{array}{c} \Delta x_{\mathrm{E}} \\ \Delta y_{\mathrm{E}} \\ \Delta z_{\mathrm{E}} \end{array} \right\|_2 . \tag{20}$$

A mapping from error sources $\Delta \boldsymbol{e}$ to the pose error of the end effector $\Delta \boldsymbol{x}_{\mathrm{E}}$ is given by (19). In order to analyze the characteristics of the transformation equation, it is recommended to normalize the individual error sources $\Delta \boldsymbol{\theta}$, $\Delta \boldsymbol{r}_{\mathrm{P}}$, $\Delta \boldsymbol{r}_{\mathrm{G}}$ as well as the ETM $\boldsymbol{K}$ [11]. After normalization, (19) can be rewritten as

$$\Delta \boldsymbol{x}_{\mathrm{E}} = \breve{\boldsymbol{K}} \Delta \breve{\boldsymbol{e}}, \tag{21}$$

where

$$\begin{aligned} \breve{\boldsymbol{K}} = \Bigg(& \boldsymbol{J} \left\| \Delta \boldsymbol{\theta} \right\|_{\max}, \; -\boldsymbol{J} \begin{pmatrix} \boldsymbol{N}_{1,1..3} \left\| \Delta \boldsymbol{r}_{\mathrm{P}} \right\|_{\max} \\ \boldsymbol{N}_{1,4..6} \left\| \Delta \boldsymbol{r}_{\mathrm{G}} \right\|_{\max} \end{pmatrix} \\ & - \cdots - \boldsymbol{J} \begin{pmatrix} \boldsymbol{N}_{6,30..33} \left\| \Delta \boldsymbol{r}_{\mathrm{P}} \right\|_{\max} \\ \boldsymbol{N}_{6,34..36} \left\| \Delta \boldsymbol{r}_{\mathrm{G}} \right\|_{\max} \end{pmatrix} \Bigg), \end{aligned} \tag{22}$$

and

$$\Delta \breve{\boldsymbol{e}} = \left(\Delta \breve{\boldsymbol{\theta}}^{\mathrm{T}}, \, \Delta \breve{\boldsymbol{r}}_{\mathrm{P}\,1..3}^{\mathrm{T}}, \, \Delta \breve{\boldsymbol{r}}_{\mathrm{G}\,1..3}^{\mathrm{T}}, \, \ldots, \, \Delta \breve{\boldsymbol{r}}_{\mathrm{G}\,16..18}^{\mathrm{T}} \right)^{\mathrm{T}} . \tag{23}$$

Here, $\|\cdot\|_{\max}$ and $\breve{\cdot}$ represent the maximum value and the normalized vector of each error source, respectively. Furthermore, $\boldsymbol{M}_{i,j..k}$ denotes the elements of the i-th row and j-th to k-th columns of a matrix $\boldsymbol{M}$, and $\boldsymbol{m}_{j..k}$ the elements of the j-th to k-th rows of a vector $\boldsymbol{m}$.

It is important to note that, generally, the manipulator Jacobian should be homogenized in order to obtain an ETM invariant of the length units adopted. As it will be explained in the following, the homogenization of $\boldsymbol{J}$ can be omitted in the here considered case.

The error transformation (21) is characterized by the six singular values $\sigma_1(\breve{\boldsymbol{K}})$, …, $\sigma_6(\breve{\boldsymbol{K}})$ of $\breve{\boldsymbol{K}}$, which are commonly referred to as Error Amplification Factors (EAFs). The smaller the EAF, the smaller the pose error [11]. With respect to the drilling task, the position error at the target (20) is considered the most relevant performance index of the parallel mechanism. Therefore, only a representative subset of $\breve{\boldsymbol{K}}$, defined as

$$\widetilde{\boldsymbol{K}} = \begin{pmatrix} \breve{\boldsymbol{K}}_1 \\ \breve{\boldsymbol{K}}_2 \\ \breve{\boldsymbol{K}}_3 \end{pmatrix}, \quad \breve{\boldsymbol{K}}_i = (k_{i,1}, \ldots, k_{i,42}), \tag{24}$$

is used for the design optimization. This is due to the fact that the singular values of $\widetilde{\boldsymbol{K}}$ characterize the mapping of input errors $\Delta \overline{\boldsymbol{e}}$ to the elements of $\Delta \boldsymbol{r}_{\mathrm{t}}$. In order to minimize the error at the target, the cost function is defined as:

$$\hat{\boldsymbol{\epsilon}} = \arg \min_{\boldsymbol{\epsilon}} \sum_{i=1}^{3} \sigma_i(\widetilde{\boldsymbol{K}}), \tag{25}$$

where $\boldsymbol{\epsilon}$ is the set of optimization parameters including the design variables r_{P}, a_x, a_y, the redundant degrees of freedom of the end effector h_{P} and γ_{E} as well as the strut-joint pairings $\mathbf{P}_{\mathrm{sel}}$.

Note that the angular errors $\Delta\alpha_{\mathrm{E}}$, $\Delta\beta_{\mathrm{E}}$, and $\Delta\gamma_{\mathrm{E}}$ are not included in the above equation and, therefore, the homogenization of $\boldsymbol{J}$ can be omitted. An upper bound imposed on the rotational deviations is considered sufficient here. Therefore, an inequality constraint is formulated. The errors $\Delta\alpha_{\mathrm{E}}$, $\Delta\beta_{\mathrm{E}}$, and $\Delta\gamma_{\mathrm{E}}$ are represented as a rotation φ_a around an axis $\boldsymbol{a}$. Then, the translational deviation d_φ from the desired trajectory can be computed at any specific distance d_{t} from the target point using

$$d_\varphi = d_{\mathrm{t}} \tan(\varphi_a) . \tag{26}$$

Here, $d_{\mathrm{t}} = z_{\mathrm{E}} = 10\,\mathrm{mm}$ corresponds to the approximate distance of the facial nerve from the target point.

The optimization problem is further constrained due to self collisions between the struts. Moreover, mechanical interference between the latter and the surgical tool must be avoided. Therefore, the struts as well as the tool are modeled by cylindrical segments having a diameter of 10 mm. Using an algorithm proposed by Merlet [18], [19], the minimum distances $d_{i,j}$ and $d_{i,\mathrm{tool}}$ between a pair of segments and between the struts and the surgical tool, respectively, can be computed. Note that, due to the described modifications of the kinematics, connected strut pairs do not require self collision monitoring. Additional constraints result from the redundant end effector DOFs being limited to $30\,\mathrm{mm} \leq h_{\mathrm{P}} \leq 100\,\mathrm{mm}$ and $0 \leq \gamma_{\mathrm{E}} \leq 2\pi$, respectively. Furthermore, in order to obtain practical results, the strut lengths are restricted to positive values $\geq 1\,\mathrm{mm}$. The optimization problem can be summarized as follows:

$$\begin{aligned} \underset{\boldsymbol{\epsilon}}{\text{minimize}} \quad & \sum_{i=1}^{3} \sigma(\widetilde{\boldsymbol{K}})_i \\ \text{subject to} \quad & d_\varphi \leq 0.1\,\mathrm{mm}, \\ & d_{i,j} \geq 1\,\mathrm{mm}, \\ & d_{i,\mathrm{tool}} \geq 1\,\mathrm{mm}, \\ & 30\,\mathrm{mm} \leq h_{\mathrm{P}} \leq 100\,\mathrm{mm}, \\ & 0 \leq \gamma_{\mathrm{E}} \leq 2\pi, \\ & \rho_i \geq 1\,\mathrm{mm}. \end{aligned} \tag{27}$$

C. Distributions of bone anchor locations and trajectories

In order to obtain realistic input data for the design optimization, a set of 20 clinical CT scans is analyzed. Drill trajectory planning is carried out on these image datasets. Each trajectory is characterized by the entry point of the drill $\boldsymbol{r}_{\mathrm{e}}$ and the target point $\boldsymbol{r}_{\mathrm{t}}$, i.e., the desired cochleostomy site. Then, appropriate locations for implanting the anchors are identified using a software that provides a measure of the skull thickness [20]. Here, regions providing skull thickness $\geq 5\,\mathrm{mm}$ are considered suitable for bone screw placement. Three regions per CT scan are defined, which corresponds to the number of required anchors. Finally, the suitable regions as well as the planned trajectories are registered and expressed in one single coordinate frame. Based on these data, the statistical distributions of suitable bone anchor locations and corresponding drill trajectories can be defined.

Here, it is assumed that each region is characterized by points that are three-variate normally distributed. Therefore, a compact representation of each region is obtained by fitting a three-variate normal distribution using the method of moments. The same procedure is carried out for the entry and target points of the planned trajectories. Once the distribution parameters are known, an arbitrary number of representative planning datasets (each comprising three bone anchor locations and one drill trajectory) can be generated.

D. Error parametrization

The proposed approach to design optimization requires the error sources involved in (19) to be parametrized appropriately. Here, the locations of the base joints $\boldsymbol{r}_{\mathrm{G}_i}$ are subject to errors occurring during the localization in a CT scan of the patient's skull. In the field of medical image registration, this is commonly referred to as the Fiducial Localization Error (FLE) [21]. In previous experiments, it was found that a base joint $\mathrm{FLE}_{\mathrm{G}_i}$ of approximately $0.06\,\mathrm{mm}$ can be achieved using steel spheres with a diameter of $8\,\mathrm{mm}$ and a flat-panel, cone-beam CT scanner (Xoran xCAT® ENT, Xoran Technologies, Ann Arbor, MI, USA) which has an isotropic resolution of $0.3\,\mathrm{mm}$ x $0.3\,\mathrm{mm}$ x $0.3\,\mathrm{mm}$ [22]. According to the widely accepted error theory, $\Delta\mathrm{G}_{i,x}$, $\Delta\mathrm{G}_{i,y}$, and $\Delta\mathrm{G}_{i,z}$ are modeled as random, independent vectors of $\mathrm{FLE}_{\mathrm{G}_i}$, whose elements are statistically independent and drawn from a three-variate normal distribution with zero means $\boldsymbol{\mu}_{\Delta\mathrm{G}}$ and the variance matrix $\boldsymbol{\Sigma}_{\Delta\mathrm{G}}$ stated in Tab. I [23]. Note that the diagonal elements of $\boldsymbol{\Sigma}_{\Delta\mathrm{G}}$ are defined as $\sigma_{1,1}^2 = \sigma_{2,2}^2 = \sigma_{3,3}^2 = {}^{\mathrm{FLE}_{\mathrm{G}_i}^2}/_3$. Due to the modified kinematics, the number of base joints being localized in a CT scan is reduced to three. Therefore, in the following, $\Delta\boldsymbol{r}_{\mathrm{G}_1} = \Delta\boldsymbol{r}_{\mathrm{G}_2}$, $\Delta\boldsymbol{r}_{\mathrm{G}_3} = \Delta\boldsymbol{r}_{\mathrm{G}_4}$, and $\Delta\boldsymbol{r}_{\mathrm{G}_5} = \Delta\boldsymbol{r}_{\mathrm{G}_6}$.

A similar formulation is established considering the locations $\boldsymbol{r}_{\mathrm{P}_i}$ of the platform joints, which are affected by manufacturing tolerances. In the here considered case, it is assumed that the positions of P_i can be measured after fabrication using a Faro GagePlus coordinate measuring machine (Faro Technologies Inc., Lake Mary, FL, USA) which has an isotropic $\mathrm{FLE}_{\mathrm{P}_i}$ of $0.025\,\mathrm{mm}$.

The strut length inaccuracies are taken from datasheets and measure $0.006\,\mathrm{mm}$. Furthermore, the limited resolution of the encoders leads to an additional round off error being $0.005\,\mathrm{mm}$ in the worst case. Therefore, $\Delta\rho_i$ is assumed to be uniformly distributed within the interval [$0\,\mathrm{mm}$, $0.011\,\mathrm{mm}$].

TABLE I

ASSUMED ERROR DISTRIBUTIONS FOR $\Delta\boldsymbol{e}$

error	distribution parameters		
$\Delta\mathrm{G}_i$	$\boldsymbol{\mu}_{\Delta\mathrm{G}_i}$	$= (0,\,0,\,0)^{\mathrm{T}}$	[mm]
	$\boldsymbol{\Sigma}_{\Delta\mathrm{G}_i}$	$= \mathrm{diag}\,({}^3/_{2500},\,{}^3/_{2500},\,{}^3/_{2500})$	[mm^2]
$\Delta\mathrm{P}_i$	$\boldsymbol{\mu}_{\Delta\mathrm{P}_i}$	$= (0,\,0,\,0)^{\mathrm{T}}$	[mm]
	$\boldsymbol{\Sigma}_{\Delta\mathrm{P}_i}$	$= \mathrm{diag}\,({}^1/_{4800},\,{}^1/_{4800},\,{}^1/_{4800})$	[mm^2]
$\Delta\rho_i$	U	$= [0,\,0.011]$	[mm]

E. Optimization strategy

The cost function defined in (25) enables an optimization of the mechanism's design variables for accuracy. However, the formulations and, therefore, the optimization results depend on the assumed configuration of the mechanism, i.e., the base joint locations and the desired drill trajectory. As already mentioned in Sect. I, this outcome is undesirable since the targeting accuracy of the PKM is increased solely for one configuration. In order to obtain practical results, a statistical approach to the design optimization is performed. The following procedure is repeated 1,000 times.

Based on the identified statistical distributions of base joint locations and corresponding drill trajectories, a random planning dataset (virtual patient) is generated. Furthermore, the entries in $\Delta\boldsymbol{e}$ are drawn from the distributions derived in Sect. III-D. The optimization problem is then formulated as described in the previous section. Initialization of the parameters is performed based on the specifications of a previous prototype [9]. In this context, all values in $\boldsymbol{\epsilon}$ are normalized to the range [0 1] to account for inhomogeneous magnitudes. Furthermore, the non-redundant coordinates of the end effector, i.e., x_{E}, y_{E}, α_{E}, and β_{E}, are set in such a way that the tool axis is aligned with the desired trajectory. Finally, the constrained optimization problem is solved using an active-set algorithm [24]. During optimization, task redundancy is exploited, i.e., the rotation around the tool axis as well as the platform height are determined. Furthermore, reconfigurability of the mechanism is considered by solving the optimization problem for each applicable set of strut-joint pairings $\mathbf{P}_{\mathrm{sel}}$ (brute force approach). The optimum set and corresponding values in $\hat{\boldsymbol{\epsilon}}$ are finally identified based on the minimum cost.

IV. RESULTS

The procedure described in Sect. III-C results in statistical distributions of bone anchor locations and trajectories. Tab. II lists the identified means $\boldsymbol{\mu}$ and corresponding variance matrices $\boldsymbol{\Sigma}$ of the assumed three-variate normal distributions.

The optimization problem formulated in Sect. III-B is solved for the 1,000 considered virtual patients. This yields one optimized robot configuration $\hat{\boldsymbol{\epsilon}}_i$ per planning dataset. In 166 cases, no valid solution is obtained due to self collisions of the struts or interference between the latter and the surgical tool. The cause lies in partially overlapping distributions of base joint G_1 and the entry point e of the drill trajectory (see also Tab. II). If the distance between these two points is less than $10\,\mathrm{mm}$, the optimization problem has no valid solution due to the continuous collision monitoring. However, considering clinical application, this represents an unrealistic scenario. Therefore, the evaluation is performed based on the remaining 834 sets of optimization results $\hat{\boldsymbol{\epsilon}}_i$. Fig. 3 gives the observed density data of $a_{\mathrm{offset}} = \|(a_x,\,a_y)\|_2$ represented as normalized histogram, i.e., the total area equals one. It corresponds to the frequency distribution of the design variable obtained through the optimization procedure. The range of this parameter lies within the interval [$2.6\,\mathrm{mm}$

TABLE II

ESTIMATED PROBABILITY DISTRIBUTIONS OF BASE JOINT LOCATIONS AND TRAJECTORIES

	distribution parameters	
G_1	$\boldsymbol{\mu}_{G_1} = (-1.575,\ -10.829,\ 11.920)^T$	[mm]
	$\boldsymbol{\Sigma}_{G_1} = \begin{pmatrix} 4.970 & 7.629 & -5.757 \\ 7.629 & 18.380 & -5.785 \\ -5.757 & -5.785 & 21.975 \end{pmatrix}$	$[\text{mm}]^2$
G_3	$\boldsymbol{\mu}_{G_3} = (15.677,\ -39.609,\ -24.915)^T$	[mm]
	$\boldsymbol{\Sigma}_{G_3} = \begin{pmatrix} 39.783 & 43.724 & -13.537 \\ 43.724 & 51.384 & -14.371 \\ -13.537 & -14.371 & 50.411 \end{pmatrix}$	$[\text{mm}]^2$
G_5	$\boldsymbol{\mu}_{G_5} = (3.847,\ 22.170,\ -63.599)^T$	[mm]
	$\boldsymbol{\Sigma}_{G_5} = \begin{pmatrix} 1.170 & 3.737 & 0.237 \\ 3.737 & 40.534 & -15.857 \\ 0.237 & -15.857 & 47.662 \end{pmatrix}$	$[\text{mm}]^2$
e	$\boldsymbol{\mu}_e = (0,\ 0,\ 0)^T$	[mm]
	$\boldsymbol{\Sigma}_e = \begin{pmatrix} 5.612 & -0.528 & -5.314 \\ -0.528 & 9.647 & 0.120 \\ -5.314 & 0.120 & 14.703 \end{pmatrix}$	$[\text{mm}]^2$
t	$\boldsymbol{\mu}_t = (-17.723,\ 9.882,\ -0.113)^T$	[mm]
	$\boldsymbol{\Sigma}_t = \begin{pmatrix} 1.871 & 0.309 & 0.070 \\ 0.309 & 9.208 & 0.819 \\ 0.070 & 0.819 & 10.912 \end{pmatrix}$	$[\text{mm}]^2$

164.3 mm], which is divided into 50 equally spaced bins. A similar representation considering the observed frequency distribution of r_P is given in Fig. 4.

Based on the histograms, the probability distributions of the design parameters can be estimated. It is revealed that a suitable approximation of the distribution of $\hat{a}_{\text{offset}}$ is obtained by fitting a generalized extreme value distribution [25], which is parametrized according to Tab. III. The same accounts for the observed values of $\hat{r}_P$. The final choice of the design variables is based on the assumption that the best performing mechanism is characterized by the values that are determined to be optimal for the majority of datasets.

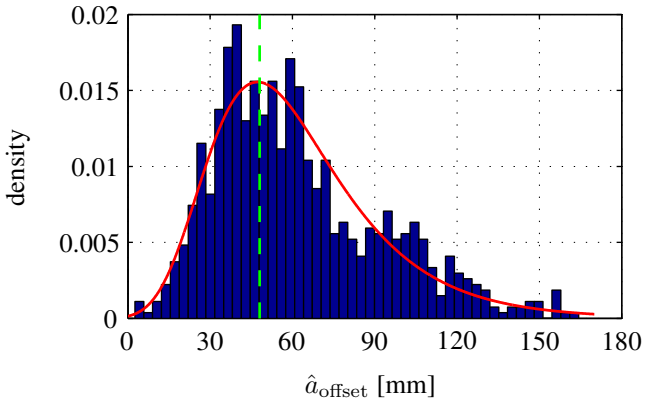

Fig. 3. Observed optimum results $\hat{a}_{\text{offset}}$: normalized histogram (blue bars) and approximated probability density function of a generalized extreme value distribution (red); the chosen value of the design variable is highlighted in green

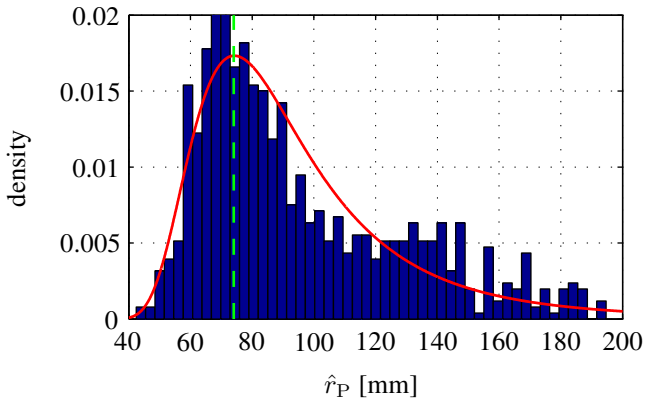

Fig. 4. Observed optimum results $\hat{r}_P$: normalized histogram (blue bars) and approximated probability density function of a generalized extreme value distribution (red); the chosen value of the design variable is highlighted in green

Therefore, the so-called location parameters μ_{GEV} of the estimated probability density functions yield the optimum design parameters $\hat{a}_{\text{offset}}$ and $\hat{r}_P$, respectively. Tab. IV lists the initially chosen as well as the optimized design variables of the parallel mechanism, which are rounded to the nearest mm for practical considerations. Due to the fact that γ_E is a redundant DOF, the obtained value of $\hat{a}_{\text{offset}}$ can be assumed in either a_x or a_y direction. In the following, $a_y = \hat{a}_{\text{offset}}$ is chosen.

In order to assess the impact of the optimized design on the accuracy at the target of each drill trajectory, a Monte Carlo simulation is carried out using the kinematic error model given in (18). All planning datasets used during the optimization (virtual patients) are evaluated by drawing 10,000 samples for $\Delta\boldsymbol{e}$ from the distributions given in Sect. III-D, and then computing $\Delta\boldsymbol{r}_t$ as defined in (20). This results in one random vector (10,000 samples of $\Delta\boldsymbol{r}_t$) per virtual patient. Therefore, the mean and standard deviation $\overline{\Delta\boldsymbol{r}_t} \pm \sigma_{\Delta\boldsymbol{r}_t}$ are computed and used for further analysis.

The accuracy evaluation is carried out comparing the following scenarios: the specific design of the parallel robot,

TABLE III

ESTIMATED PROBABILITY DISTRIBUTIONS OF THE DESIGN VARIABLES

Design variable	$\hat{a}_{\text{offset}}$	$\hat{r}_P$
Distribution	generalized extreme value	
μ_{GEV} [mm]	47.698	78.229
σ_{GEV} [mm]	23.659	21.673
ξ_{GEV} [-]	0.018	0.209

TABLE IV

INITIALLY CHOSEN AND OPTIMIZED DESIGN VARIABLES OF THE PROPOSED PARALLEL KINEMATIC MECHANISM

Design variable	initial	optimized
a_x [mm]	0	0
a_y [mm]	5.8	48.0
r_P [mm]	35.0	78.0

i.e., the optimal result $\hat{\boldsymbol{\epsilon}}_i$, for each virtual patient is considered as the gold standard (GS) with respect to accuracy. The corresponding targeting errors obtained through Monte Carlo simulation are denoted as $\Delta\boldsymbol{r}_{\mathrm{t,GS}}$. Furthermore, the simulation is repeated assuming the same virtual patients and the initial and optimized mechanism, respectively. Even though the design variables a_x, a_y, and r_{P} are constant in these scenarios, the redundant degrees of freedom of the mechanism h_{P} and γ_{E} as well as the strut-joint pairings $\boldsymbol{P}_{\mathrm{sel}}$ are optimized according to the previously defined cost function given in (25). The obtained errors at the target points of the considered trajectories are denoted as $\Delta\boldsymbol{r}_{\mathrm{t,init}}$ and $\Delta\boldsymbol{r}_{\mathrm{t,opt}}$, respectively.

Fig. 5 gives the mean targeting errors $\overline{\Delta\boldsymbol{r}_{\mathrm{t}}}$ and corresponding standard deviations $\sigma_{\Delta\boldsymbol{r}_{\mathrm{t}}}$ for an arbitrarily chosen subset of ten virtual patients. It is revealed that the initial, intuitively designed mechanism exhibits the largest targeting errors in all cases. Thanks to the proposed optimization procedure, the targeting errors as well as the standard deviations determined by Monte Carlo simulation are significantly reduced. The accuracy of the optimized manipulator design is slightly inferior to the gold standard, i.e., the patient specific mechanism design.

The frequency distributions of the mean targeting errors, resulting when analyzing the total number of virtual patients, are given in Fig. 6 for the three considered scenarios. Note that, in this representation, the standard deviations $\sigma_{\Delta\boldsymbol{r}_{\mathrm{t}}}$ of the errors are omitted. Again, the gold standard mechanisms provide the highest targeting accuracies. The mean and the standard deviation of the observed $\Delta\boldsymbol{r}_{\mathrm{t,GS}}$ are $(0.059 \pm 0.007)\,\mathrm{mm}$. The mean targeting error of the optimized mechanism with constant design parameters is slightly larger, being $(0.065 \pm 0.014)\,\mathrm{mm}$. Compared to the intuitively defined mechanism, which, according to the simulation results, provides a mean accuracy of $(0.110 \pm 0.027)\,\mathrm{mm}$, the targeting error is reduced by approximately $40\,\%$ through the proposed design optimization.

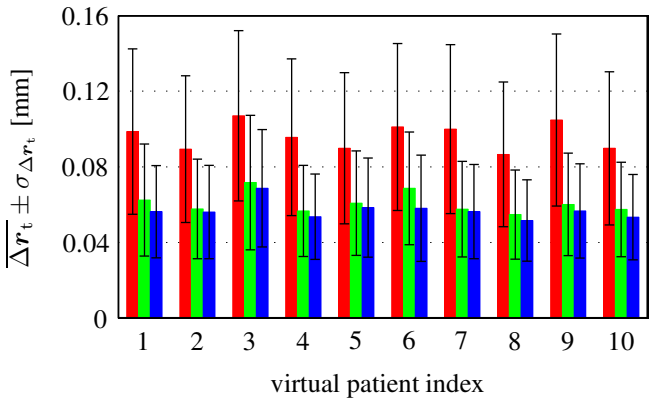

Fig. 5. Results of Monte Carlo simulation: mean targeting errors and corresponding standard deviations of gold standard (blue bars), optimized (green bars) and initial (red bars) mechanism design

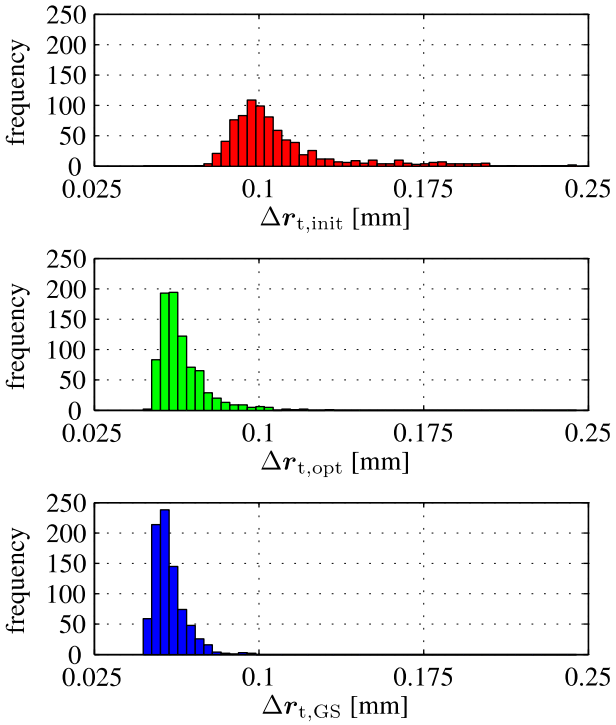

Fig. 6. Frequency distributions of the mean targeting errors: initial (red bars), optimized (green bars), and gold standard (blue bars) mechanism designs

V. CONCLUSIONS AND FUTURE WORK

In this paper, a novel, statistical approach to the design optimization of a parallel mechanism for skull surgery is presented. Compared to previous studies, the given task redundancy of the mechanism as well as its reconfigurability are taken into account. For this purpose, a kinematic model including all relevant error sources is used. The latter are represented using probability distributions which approximate experimental data. Furthermore, with respect to the here considered application, the range of possible base joint locations and corresponding trajectories has been determined and expressed accordingly. Hence, all input parameters of the kinematic error model are given by one consistent representation. As a result, an arbitrary number of realistic planning datasets (virtual patients), including base joints, a trajectory and an error source vector, can be generated based on the previously identified statistical distributions. Here, the optimum design parameters of the parallel mechanism's platform are determined by minimization of the error amplification factors for a set of 1,000 virtual patients, and subsequent analysis of the resulting frequency distributions. The achievable targeting accuracy is then evaluated by Monte Carlo simulation. Results reveal that the proposed approach reduces the mean targeting errors by approx. $40\,\%$ with respect to an intuitively chosen mechanism design previously proposed.

Compared to patient specific mechanism designs, which we consider the gold standard with respect to targeting accuracy, the optimized mechanism resembles the best achievable

compromise. With that in mind, the difference in the mean targeting accuracy is relatively small. This is due to the fact that exploiting the given task redundancy and reconfigurability of the mechanism has a significant effect on its performance. As the results reveal, minor deviations from the patient specific design optimum can be compensated for in terms of the achievable targeting accuracy.

In future work we intend to study the effect of including more design variables, e.g., the platform joint locations $\boldsymbol{r}_{\mathrm{P}_i}$, in the proposed procedure. Finally, a prototype has to be built based on the resulting specifications to enable experimental evaluation of the achievable targeting accuracy.

REFERENCES

[1] S. Baron, H. Eilers, B. Munske, J. L. Toennies, R. Balachandran, R. F. Labadie, T. Ortmaier, and R. J. Webster, "Percutaneous inner-ear access via an image-guided industrial robot system," *Proc. of the Institution of Mechanical Engineers Part H: Journal of Engineering in Medicine*, vol. 224, no. 5, pp. 633 – 649, May 2010.

[2] R. F. Labadie, J. Mitchell, R. Balachandran, and J. M. Fitzpatrick, "Customized, rapid-production microstereotactic table for surgical targeting: description of concept and in vitro validation," *Int J CARS*, vol. 4, no. 3, pp. 273 – 280, 2009.

[3] O. Majdani, T. Rau, S. Baron, H. Eilers, C. Baier, B. Heimann, T. Ortmaier, S. Bartling, T. Lenarz, and M. Leinung, "A robot-guided minimally invasive approach for cochlear implant surgery: preliminary results of a temporal bone study," *Int J CARS*, vol. 4, no. 5, pp. 475 – 486, Sep. 2009.

[4] T. Klenzner, C. Ngan, F. Knapp, H. Knoop, J. Kromeier, A. Aschendorff, E. Papastathopoulos, J. Raczkowsky, H. Wörn, and J. Schipper, "New strategies for high precision surgery of the temporal bone using a robotic approach for cochlear implantation," *Eur Arch Otorhinolaryngol*, vol. 266, no. 7, pp. 955 – 960, Jul. 2009.

[5] J. Schipper, A. Aschendorff, I. Arapakis, T. Klenzner, C. B. Teszler, G. J. Ridder, and R. Laszig, "Navigation as a quality management tool in cochlear implant surgery," *J Laryngol Otol*, vol. 118, pp. 764 – 770, 2004.

[6] L. B. Kratchman, G. S. Blachon, T. J. Withrow, R. Balachandran, R. F. Labadie, and R. J. Webster, "Design of a bone-attached parallel robot for percutaneous cochlear implantation," *IEEE T. Bio-Med. Eng.*, vol. 58, no. 10, pp. 2904 – 2910, Oct. 2011.

[7] L. B. Kratchman and J. M. Fitzpatrick, "Robotically-adjustable microstereotactic frames for image-guided neurosurgery," in *Proc. SPIE 8671, Medical Imaging*, 2013, pp. 86 711U–86 711U–11.

[8] R. F. Labadie, R. Balachandran, J. Mitchell, J. H. Noble, O. Majdani, D. Haynes, M. Bennett, B. M. Dawant, and J. M. Fitzpatrick, "Clinical validation study of percutaneous cochlear access using patient-customized microstereotactic frames," *Otology & Neurotolgy*, vol. 31, no. 1, p. 94, Jan. 2010.

[9] J.-P. Kobler, J. Kotlarski, J. Öltjen, S. Baron, and T. Ortmaier, "Design and analysis of a head-mounted parallel kinematic device for skull surgery," *Int J CARS*, vol. 7, no. 1, pp. 137 – 149, Jan. 2012.

[10] O. Ma and J. Angeles, "Optimum architecture design of platform manipulators," in *Fifth Int. Conf. on Advanced Robotics*, vol. 2, 1991, pp. 1130 – 1135.

[11] J. Ryu and J. Cha, "Volumetric error analysis and architecture optimization for accuracy of hexaslide type parallel manipulators," *Mechanism and Machine Theory*, vol. 38, no. 3, pp. 227 – 240, 2003.

[12] Q. Xu and Y. Li, "Error analysis and optimal design of a class of translational parallel kinematic machine using particle swarm optimization," *Robotica*, vol. 27, pp. 67 – 78, 2009.

[13] R. Kelaiaia, O. Company, and A. Zaatri, "Multiobjective optimization of parallel kinematic mechanisms by the genetic algorithms," *Robotica*, vol. 30, pp. 783 – 797, 2012.

[14] C. M. Gosselin and J. Angeles, "Singularity analysis of closed-loop kinematic chains," *IEEE Trans. Robot. Autom.*, vol. 6, no. 3, pp. 281 – 290, June 1990.

[15] J.-P. Merlet, "Computing the worst case accuracy of a PKM over a workspace or a trajectory," in *Proc. of the 5th Chemnitz Parallel Kinematics Seminar*, April 2006, pp. 83 – 96.

[16] T. Ropponen and T. Arai, "Accuracy analysis of a modified stewart platform manipulator," in *Proc. of the IEEE Int. Conf. on Robotics and Automation*, vol. 1, 1995, pp. 521 – 525.

[17] A. Patel and K. Ehmann, "Volumetric error analysis of a Stewart platform-based machine tool," *CIRP Annals - Manufacturing Technology*, vol. 46, no. 1, pp. 287 – 290, 1997.

[18] J.-P. Merlet, *Parallel Robots (Second Edition)*, J.-P. Merlet, Ed. Dordrecht, Niederlande: Springer, 2006.

[19] ——, "Determination of the workspace of a parallel manipulator for a fixed orientation," *Mechanism and Machine Theory*, vol. 29, no. 8, pp. 1099 – 1113, 1994.

[20] G. J. Lexow, T. S. Rau, F. Eckardt, J.-P. Kobler, T. Ortmaier, T. Lenarz, M. Leinung, and O. Majdani, "Automatisierte Bestimmung der Schädelknochendicke in CT- und DVT-Bilddaten," in *Tagungsband der 11. Jahrestagung der Deutschen Gesellschaft für Computer- und Roboterassistierte Chirurgie e.V. (CURAC)*, 2012.

[21] J. M. Fitzpatrick, J. B. West, and J. C. R. Maurer, "Predicting error in rigid-body point-based registration," *IEEE Trans. Med. Imag.*, vol. 17, no. 5, pp. 694 – 702, 1998.

[22] J.-P. Kobler, J. Diaz Diaz, J. M. Fitzpatrick, G. J. Lexow, O. Majdani, and T. Ortmaier, "Localization accuracy of sphere fiducials in computed tomography images," in *SPIE Medical Imaging*, 2014.

[23] J. M. Fitzpatrick, "Fiducial registration error and target registration error are uncorrelated," in *Proc. SPIE 7261, Medical Imaging*, 2009, pp. 726 102–726 102–12.

[24] J. Nocedal and S. J. Wright, *Numerical Optimization*. Springer New York, 2006.

[25] S. I. Resnick, *Extreme Values, Regular Variation and Point Processes*, T. V. Mikosch, S. M. Robinson, and S. I. Resnick, Eds. Springer, 1987.